Electrically controlled topological defects in liquid crystals as tunable spin-orbit encoders for photons

Etienne Brasselet* and Charles Loussert

Laboratoire Ondes et Matière d'Aquitaine, Université Bordeaux 1, CNRS, 351 Cours de la Libération, 33405 Talence Cedex, France
**Corresponding author: e.brasselet@cpmoh.u-bordeaux1.fr*

Received January 3, 2011; accepted January 19, 2011;
posted February 1, 2011 (Doc. ID 140306); published February 28, 2011

We demonstrate experimentally that topological defects of vertically aligned nematic liquid crystal films induced by electric fields can be used as highly efficient natural optical spin-orbit encoders that do not need machining techniques. Moreover, we show that both the operating wavelength and operation mode of such natural quantum optical interfaces can be tuned in real time using low-voltage electric fields.

OCIS codes: 160.1190, 230.3720, 260.6042.

During the last decade liquid crystals have naturally found their place in singular optics [1,2] as anisotropic optical materials. Indeed their long-range orientational order and high birefringence allow the design of optical elements that are able to modify the phase spatial profile of a light field. In particular, the coupling between the spin and orbital contributions to the total angular momentum of light, the optical spin-orbit coupling, is a prime phenomenon.

A widespread example consists of azimuthally patterned nematic films where the local averaged molecular axis orientation (called the director) in the plane of the film, represented by the angle θ, continuously varies around an origin point as a function of the azimuthal coordinate φ, $\theta = m\varphi + \theta_0$, with m integer or half-integer. For this purpose, various surface and bulk strategies have been proposed. Mechanical circular rubbing of polymer-coated substrates [3] ($m = 1$, $\theta_0 = \pi/2$) or optical patterning of photosensitive polymer coated substrates [4] ($m = \{1/2, 1, 3/2\}$, $\theta_0 = 0$) are examples of the surface type whereas bulk approaches have been achieved using electrical radial realignment [5] ($m = 1$, $\theta_0 = 0$) or optical axial realignment [6] ($m = 1$, $-\pi/2 < \theta_0 < \pi/2$).

The ability to generate light beams carrying phase singularities from nonsingular beams, e.g. Gaussian beams, using two-dimensional patterned birefringent systems was first demonstrated for mid-infrared wavelength owing to the form birefringence of subwavelength gratings [7], and later for visible wavelength owing to the natural birefringence liquid crystals [8]. Although the use of liquid crystals is significant in terms of ease of manufacture, their self-organization properties have been barely used up to now despite their technology-free potential. To our knowledge, edge dislocations in cholesteric films [9] and point defects in nematic droplets [10] are the only two examples. However, none of these "natural" approaches is able to allow for a fully controlled spin-orbit manipulation of photons, which has been restricted so far to the use of artificial liquid crystal spin-orbit couplers [11].

Here we show that electrically generated topological defects in vertically aligned nematic liquid crystal films can be used as highly efficient optical spin-orbit encoders. Moreover, we demonstrate that both the operating wavelength and operation mode of such natural quantum optical interfaces can be tuned in real-time using low-voltage electric fields.

In experiments we used a $L = 15\,\mu$m-thick nematic film, which defines the (x, y) plane, sandwiched between two glass substrates provided with transparent electrodes and perpendicular anchoring treatment. We chose the nematic MLC-2079 (from Licristal) with a negative dielectric anisotropy at low frequencies, $\varepsilon_a^{(\Omega)} = \varepsilon_{\parallel}^{(\Omega)} - \varepsilon_{\perp}^{(\Omega)} = -6.1$ at $\Omega = 1$ kHz, where $(\parallel, \perp)$ refer to directions parallel and perpendicular to the director, respectively. Therefore, by applying a low-frequency voltage between the two electrodes, the director tends to align perpendicularly to the electric field. Since the initial alignment along z is azimuthally degenerated, topological defects spontaneously appear all over the film; see Fig. 1(a). They correspond to umbilics, of strength $m = \pm 1$, around which the director field changes not only along the z axis but also along the radial coordinates [12]. Such three-dimensional features, which have already been determined experimentally by fluorescence confocal polarizing microscopy [13], vary with the electric field amplitude and are associated with $\theta = \pm\varphi + \theta_0$ [12].

The visualization of umbilical defects is easily made from cross-polarized imaging, as shown in Fig. 1(a)

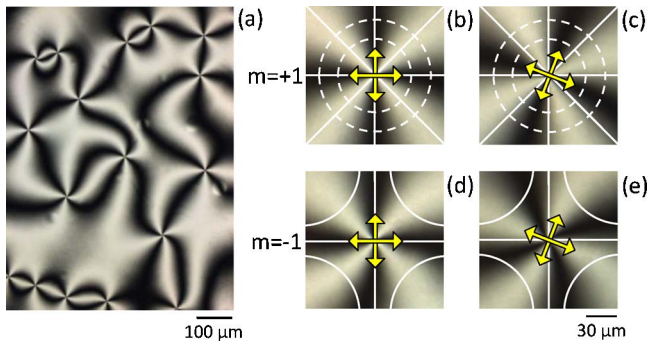

Fig. 1. (Color online) (a) Cross-polarized white light imaging of defects under $25\,V_{rms}$ voltage. (b), (c) and (d), (e) $m = \pm 1$ defects, respectively. White lines represent the geometry of the transverse part of the director field with two possible cases when $m = +1$ [12]; see solid (splay-type umbilic) and dashed (twist-type umbilic) lines. Arrows indicate the direction of the pair of polarizers for a small clockwise rotation from (b) to (c) and (d) to (e).

where each of the dark cross centers corresponds to the location of a defect. In addition, it is possible to distinguish between $m = \pm 1$ defects: a clockwise rotation of the pair of crossed polarizers makes the image of the $m = +1$ defects rotate in a clockwise direction, see Figs. 1(b) and 1(c), whereas it rotates counterclockwise when $m = -1$, see Figs. 1(d) and 1(e).

The spin-to-orbital light angular momentum conversion operated by the topological defects is illustrated in Fig. 2. Figure 2(a) presents the intensity distribution obtained between crossed circular polarizers (that are combinations of a polarizer and a quarter wave plate) under uniform white light illumination. The observed dark core is associated with the presence of an optical vortex embedded in the contra-polarized component of the output field with respect to the polarization state of the incident light field. This is further confirmed in Fig. 2(b) that shows the spatial phase distribution of such an optical vortex, Φ. The latter is retrieved from the spatially resolved polarimetric analysis of the total output field under circularly polarized illumination, as detailed in [10]. Actually, we have $\Phi = \arctan[(I_{+45^\circ} - I_{-45^\circ})/(I_{0^\circ} - I_{90^\circ})]$, where I_α refers to the intensity distribution obtained by placing a polarizer at an angle α from the x axis at the output of the film. A radially symmetric 4π phase change per full rotation around the defect is observed whatever is the selected wavelength. This concludes to the generation of a charge-two white light optical vortex located at the place of the umbilic.

The spin-to-orbital conversion efficiency, η, is defined as the power fraction of an incident circularly polarized light field that is converted into an optical vortex beam. It is known to strongly depend on the wavelength [14], which rules out the blind use of topological defects as spin-orbit optical encoders that require $\eta = 1$, i.e. a total phase delay $\Delta = (2n + 1)\pi$ associated with the birefringence, with n integer [8]. We propose adjusting the amplitude of the electric field that gave rise to the topological defect in order to provide an optimal optical spin-orbit behavior for the chosen operating wavelength λ.

The experimental dependence of $\eta(U)$ is retrieved by using a Gaussian laser beam (characterized by a waist $\sim 20\,\mu$m at sample location) normally incident on the film and centered on a defect. As it is expected from a uniformly aligned liquid crystal film with vertical alignment, the optical spin-orbit conversion efficiency is $\eta = 0$ below the reorientation voltage threshold $U_F \sim 1.9\ V_{rms}$

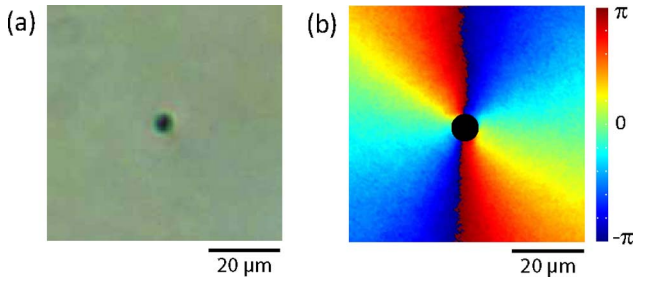

Fig. 2. (Color online) (a) Cross-circularly-polarized white light imaging of a topological defect. (b) Phase spatial profile of the contra-circularly polarized component of the output field with respect to the incident-circularly polarized light beam, here measured at $\lambda = 532$ nm.

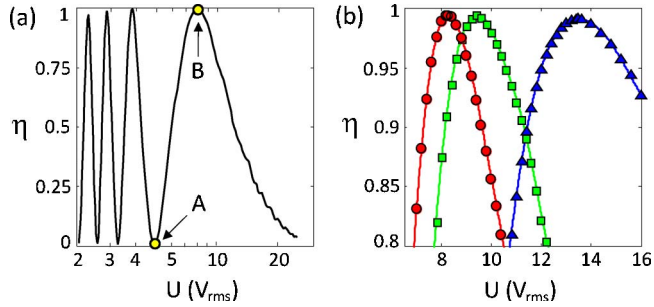

Fig. 3. (Color online) (a) Measured η versus U at $\lambda = 632.8$ nm. Labels A and B refer to extremum values $\eta_{min} \simeq 0$ and $\eta_{max} \simeq 1$, respectively. (b) Electrical tuning of the operating wavelength to the operation mode that corresponds to $\eta = 1$ for red ($\lambda = 632.8$ nm, circles), green ($\lambda = 532$ nm, squares) and blue ($\lambda = 488$ nm, triangles) wavelength. The solid curves are splines to guide the eyes.

($\Omega = 2$ kHz in experiments). Such a threshold behavior corresponds to the electric field-induced Fréedericksz transition characterized by $U_F = \pi[K_3/(\varepsilon_0|\varepsilon_a^{(\Omega)}|)]^{1/2}$, which gives $U_F = 1.83\ V_{rms}$ by using the datasheet value of the dielectric permittivity at 1 kHz and $K_3 = 18.3$ pN, where K_3 is the Frank bend elastic constant and ε_0 is the vacuum permittivity. For $U > U_F$, η oscillates as U is increased; see Fig. 3(a). This oscillating behavior eventually saturates when $U \gg U_F$, which corresponds to a maximal liquid crystal reorientation angle $\pi/2$ (with respect to the z axis) in the whole bulk film apart from tiny regions near the cell walls. More precisely, $\eta(U)$ experiences $N = (n_\parallel - n_\perp)(L/\lambda)$ oscillation periods to reach the saturation regime, where $n_{\parallel,\perp}$ are the refractive indices along directions parallel and perpendicular to the director. Since, from the datasheet, $n_\parallel - n_\perp = 0.15$ at $\lambda = 589.3$ nm, we get the estimated value $N \sim 3.5$, which qualitatively agrees with the observed $N \sim 4$; see Fig. 3(a).

The extremum values of η are all the more close to 0 and 1 as U increases. This can be attributed to the dependence of Δ on the distance r from the defect location. In fact the reorientation angle significantly varies only in a restricted

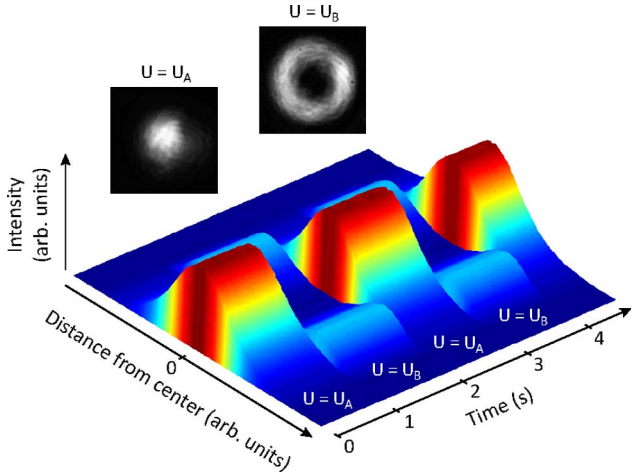

Fig. 4. (Color online) Measured intensity profile of the output light beam for a 0.5 Hz square-wave voltage between $U = U_A$ to $U = U_B$, by referring to Fig. 3(a). The reported data are obtained by averaging the experimental intensity distribution (see insets) over the azimuth.

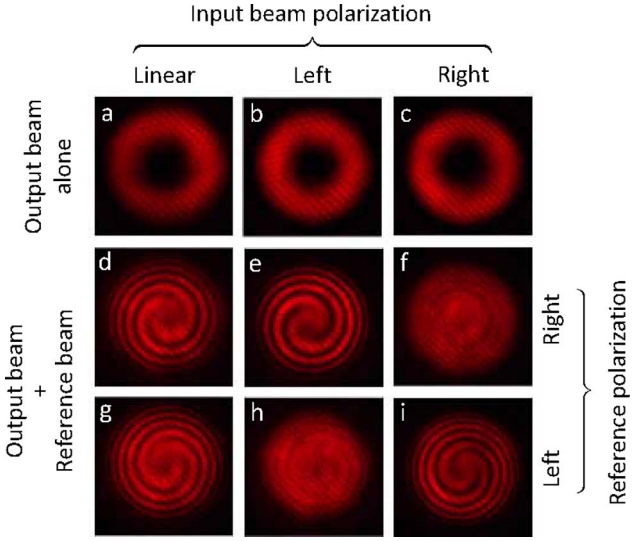

Fig. 5. (Color online) Spin-orbit encoding of photons using an electrically optimized defect at $\lambda = 632.8\,\mathrm{nm}$. The first row shows the output total intensity profile for linearly and circularly (left or right) polarized incident beam whereas the second and third rows show the interference patterns with a right- and left-handed circularly polarized reference fundamental Gaussian beam, respectively.

area around the defect, which defines the core of the umbilic whose radius that scales as $(L/\pi)(U^2/U_F^2 - 1)^{-1/2}$ [12]. Therefore, the higher the voltage U is, the smaller the size of the umbilic core is, and the more uniform is the birefringence in a given neighborhood around a defect. Experimentally, we measured a deviation less than 1% from the ideal case $\eta_{\min} = 0$ and $\eta_{\max} = 1$ whatever the wavelength as shown in Fig. 3(b) for red ($\lambda = 633\,\mathrm{nm}$), green ($\lambda = 532\,\mathrm{nm}$), and blue ($\lambda = 488\,\mathrm{nm}$) wavelengths. In addition, the real-time reconfiguration of our natural spin-orbit optical interface is also possible. This is demonstrated in Fig. 4, where the total output intensity profile dynamics is shown for a 0.5 Hz square-wave voltage between $U = U_A$ (vortex generator "off") to $U = U_B$ (vortex generator "on") where labels A and B refer to the voltage values indicated on Fig. 3(a).

When the optical spin-orbit conversion efficiency is optimized to reach the ideal value $\eta = 1$, the topological defects enable one to fully control the entanglement of the polarization of a photon with its orbital angular momentum. This is summarized in Fig. 5 where the intensity and phase features of the output beam are shown for a linearly, right- or left-handed circularly polarized incident Gaussian beam. The intensity profiles exhibit a similar doughnut shape in all cases, see Figs. 5(a)–5(c), though they are associated with distinct photon states.

On the one hand, when the input beam polarization is left- or right-circular, the output photons are respectively described by the separable states $|\mp 1\rangle_S \bigotimes |\pm 2\rangle_{L_2}$ in the spin-orbit space $S \bigotimes L_2$. Here S refers to the polarization degree of freedom associated with the right- (spin down) and left- (spin up) circular polarization basis $\{|-1\rangle, |+1\rangle\}_S$, and L_2 refers to subspace of the infinite dimensional Hilbert space of orbital angular momentum that is associated with the quantum orbital number $l = \pm 2$ and basis $\{|-2\rangle, |+2\rangle\}_{L_2}$. This can be retrieved from the interference patterns between the output beam obtained from a $\mathcal{P}_{\mathrm{in}}$-polarized incident beam and a collinear $\mathcal{P}_{\mathrm{ref}}$-polarized reference Gaussian beam, to which we further refer to as the "$\mathcal{P}_{\mathrm{in}}/\mathcal{P}_{\mathrm{out}}$" cases. Indeed, the left/left and right/right patterns do not exhibit intensity modulation, see Figs. 5(f) and 5(h), whereas two-arm spiraling fringes with maximum contrast are observed in the left/right and right/left cases as shown in Figs. 5(e) and 5(i).

On the other hand, when the input beam is linearly polarized, the polarization and the orbital angular momentum of the output photons are maximally entangled and their state is given by $(|+1\rangle_S \bigotimes |-2\rangle_{L_2} + |-1\rangle_S \bigotimes |+2\rangle_{L_2})/\sqrt{2}$. This is verified from the observation of two-arm spiraling fringes with intermediate contrast and opposite handedness in the linear/left and linear/right cases; see Figs. 5(d) and 5(g), respectively.

In conclusion, we have demonstrated that electric–field–induced topological defects in vertically aligned nematic liquid crystal films behave as highly efficient optical spin-orbit encoders whose operating wavelength and operation mode of such natural quantum optical devices can be adjusted and changed in real time using low-voltage electric fields.

References

1. M. S. Soskin and M. V. Vasnetsov, Prog. Opt. **42**, 219 (2001).
2. M. R. Dennis, K. O'Holleran, and M. J. Padgett, Prog. Opt. **53**, 293 (2009).
3. M. Stalder and M. Schadt, Opt. Lett. **21**, 1948 (1996).
4. S. C. McEldowney, D. M. Shemo, R. A. Chipman, and P. K. Smith, Opt. Lett. **33**, 134 (2008).
5. H. Ren, Y.-H. Lin, and S.-T. Wu, Appl. Phys. Lett. **89**, 051114 (2006).
6. E. Brasselet, Opt. Lett. **34**, 3229 (2009).
7. G. Biener, A. Niv, V. Kleiner, and E. Hasman, Opt. Lett. **27**, 1875 (2002).
8. L. Marrucci, C. Manzo, and D. Paparo, Phys. Rev. Lett. **96**, 163905 (2006).
9. D. Voloschenko and O. D. Lavrentovich, Opt. Lett. **25**, 317 (2000).
10. E. Brasselet, N. Murazawa, H. Misawa, and S. Juodkazis, Phys. Rev. Lett. **103**, 103903 (2009).
11. E. Nagali, F. Sciarrino, F. D. Martini, L. Marrucci, B. Piccirillo, E. Karimi, and E. Santamato, Phys. Rev. Lett. **103**, 013601 (2009).
12. A. Rapini, J. Phys. (Paris) **34**, 629 (1973).
13. M. Gu, I. I. Smalyukh, and O. D. Lavrentovich, Appl. Phys. Lett. **88**, 061110 (2006).
14. E. Brasselet, Y. Izdebskaya, V. Shvedov, A. S. Desyatnikov, W. Krolikowski, and Y. S. Kivshar, Opt. Lett. **34**, 1021 (2009).